Turbulence modulation in concentrated, high-Reynolds-number solid–liquid flows

David Breakey[1]*, Yogesh Agrawal[2], Parsa Amini[2], Sina Ghaemi[2], David Nobes[2], and R. Sean Sanders[1]

[1]*Department of Chemical and Materials Engineering, University of Alberta, Edmonton, Canada*
[2]*Department of Mechanical Engineering, University of Alberta, Edmonton, Canada*

This paper presents a refractive-index matched Particle Image Velocimetry (PIV) vertical pipe loop experiment for measuring turbulence modulation in a concentrated high-Reynolds-number flow comprising potassium thiocyanate as the liquid phase and borosilicate beads as the solid phase. The advantage of this setup is that it allows PIV to be performed at higher solid concentrations than previous experiments. The current results are restricted to a presentation of a bead-centric PIV procedure that minimizes image area lost to masking and allows the computation of the average flow in the pipe and the average flow field around the beads at various radial locations. The procedure is shown to be effective, and the initial results show that, near the pipe centre, the beads tend to lag the flow by an amount close to the terminal settling velocity and that the shape of the flow around the bead and its wake vary significantly throughout the pipe.

Keywords: Turbulence modulation, solid–liquid flow, Particle Image Velocimetry, refractive-index matching

1. Introduction

Solid–liquid flows are of significant importance to the chemical and energy industries, occurring in many different contexts. From pipes and mixing reactors in chemical production lines to slurry flows in the mining and mineral processing industry, a wide variety of flow conditions of this type can be found. Many of these flows are turbulent, and the typical complexity accompanying the study of turbulence is further complicated by the interactions between the liquid phase and the solid particles in these flows. These interactions are not well understood. For instance, in some situations adding particles to turbulent flows causes an increase in turbulence intensity (augmentation) and in others it causes a decrease (attenuation). Some criteria have been suggested to predict the circumstances under which each of these would occur, and these tend to be based on a particle size to eddy length scale ratio [1] or more complicated expressions [2]. However, these criteria do not explain the mechanism that leads to turbulence modulation, and they have only been verified for dilute flows with relatively low Reynolds numbers ($\lesssim 30\,000$) [3].

Particle Image Velocimetry (PIV) is a flow measurement technique that has been widely adopted for many flows. For multiphase flows, shadows, ghost particles, reflections, refraction effects, and glare resulting from the presence of the solid phase hinder PIV processing. Significantly, these effects are associated with the motion of the dispersed phase and they make it difficult, if not impossible, to isolate the motion of the continuous phase. This is because the reflections and glare may overlay the continuous phase areas of the image, and even though this may result in high correlation in the PIV computation, these peaks are associated with dispersed phase motion and not continuous phase motion. For flows with a dilute dispersed phase, when these effects do not significantly affect the continuous-phase portions of the image, it is possible to use a combined Particle Tracking Velocimetry (PTV) and PIV technique to isolate the motion of each phase individually [4, 5]. However, for more concentrated flows, the image artifacts associated with the dispersed phase tend to leave no unaffected areas for the PIV computation. Though it may be possible to obtain consistent vectors from the PIV software, determining if these vectors reflect the motion of the liquid phase or the dispersed phase—or some unclear combination of the two—can be difficult, and isolating either can be impossible.

A common way to overcome some of the optical issues presented by multiphase flows is to use refractive-index matching (RIM), a technique that ensures that the materials through which light passes have very similar refractive indices, reducing or eliminating diffraction and reflection at interfaces. This is a first step in permitting the use of PIV in concentrated multiphase flows. This paper presents a RIM experiment in a vertical flow loop where the dispersed (solid) phase is solid borosilicate glass beads and the continuous (liquid) phase is a solution of potassium thiocyanate (KSCN). These phases were chosen because the two can be matched to the same refractive index.

The ultimate aim of this work is a comprehensive analysis of turbulence modulation in concentrated, high-Reynolds-number flows, but due to the technical and experimental challenges described below, only the techniques required to perform valid PIV for each phase and some early results are presented here. Section 2 describes the RIM-PIV setup, and Sec. 3 presents samples of the obtained images. A new bead-centric PIV procedure that optimizes mask placement and vector computation is presented in Sec. 4. The results of this work are discussed in Sec. 5, and Sec. 6 makes suggestions for the next steps in this investigation.

2. Experimental setup

The experiments were performed in a uniquely designed pilot-scale vertical flow loop facility with $D = 50.6$ mm. The facility has been modified from its previously reported form [4, 5] to measure the turbulence statistics in more concentrated solid–liquid flows, requiring the capacity to handle a toxic, abrasive, and corrosive liquid phase. An overview of the experimental setup is shown in Fig. 1.

The index-matched solution was prepared in a mixing tank (1) and further transferred into a feed tank (2) using a 0.5 HP peristaltic pump (11; Cole-Parmer Masterflex B/T 91). The slurry was pumped using a corrosive-resistant rotary lobe pump (3; Lobe Pro CM50) connected to a variable frequency drive (Schneider Electric Altivar 61) and a 20 HP electric motor. The vertical loop was isolated from the feed tank and operated in closed loop

*Corresponding author: david.breakey@ualberta.ca. This work has been funded by the Natural Sciences and Engineering Research Council of Canada (NSERC), Canadian Natural Resources Limited, Nexen Inc., Paterson & Cooke Canada Inc., Shell Canada Energy, Saskatchewan Research Council, Suncor Energy Inc., Syncrude Canada Ltd., Teck Resources Ltd., and Total American Services through the NSERC Industrial Chair in Pipeline Transport Processes (RSS).

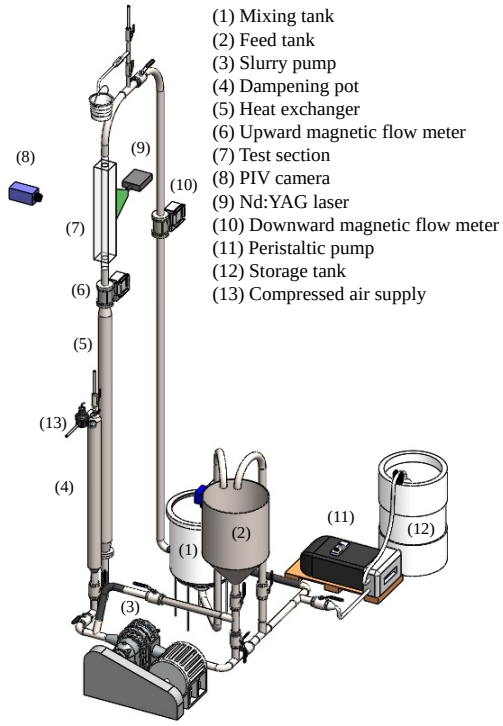

Figure 1: Experimental setup for vertical flow loop

(recirculating) mode after loading the slurry. A dampening pot (4) was installed to absorb pulses generated by the pump and to pressurize the loop to avoid cavitation. The dampening pot was pressurized from a compressed air supply line (13). A double-pipe heat exchanger (5) was installed to maintain the temperature of the slurry at 25°C. The slurry flow rate was measured using two electromagnetic flow meters (6, 10; Foxboro 9200A-IMT25) located in both the upstream and downstream sections of the loop. The test section was located at a streamwise position of 90 D from the bottom bend in an attempt to obtain fully developed turbulent flow. A standard commercial planar PIV system was used to acquire the images. The PIV system consisted of a double-pulse Nd:YAG laser @ 532 nm (9; New Wave Solo III-15z) to illuminate the flow, light-sheet-forming optics, and a 1376 × 1040 pixel CCD camera (8; LaVision Imager Intense) for imaging. The magnification was such that the scale was 0.0384 mm/px. Silver-coated hollow spherical particles were used for seeding (2 μm diameter, $\rho = 2200$ kg/m^3, Potters Industries SG02S40). The seeding particles were considered small enough to track the flow. The PIV measurements were performed in a transparent test section (7) to allow optical access. A central timing unit was configured to control and synchronize the timing signal between two images, and dt was set to 70 μs, corresponding to a pixel shift on the order of 8 px. Statistically independent double-frame PIV images were recorded at 1.7 Hz (5000 images). After completion of the PIV measurements, the slurry was discharged back to a storage tank (12) using the peristaltic pump (11).

The solid–liquid slurry consisted of an aqueous KSCN solution (62.4% w/w, $\rho = 1380$ kg/m^3, $\mu = 2.2$ mPa·s) with a refractive index of $n = 1.4703$ at 25°C and 3 mm Borosilicate glass beads ($\rho = 2230$ kg/m^3) with a refractive index of $n = 1.4730$. The bead concentration was 5% v/v. The average mixture velocity was 4.6 m/s, corresponding to a Reynolds number (based on the fluid properties) of 148 000. To compare the quality of the RIM images to a non-RIM solid–liquid flow, a set of measurements was also obtained using a 5% v/v concentration of 3 mm glass beads ($\rho = 2500$ kg/m^3, $n = 1.51$) in water ($\rho = 997$ kg/m, $\mu = 0.890$ mPa·s, $n = 1.3326$), also at 25°C.

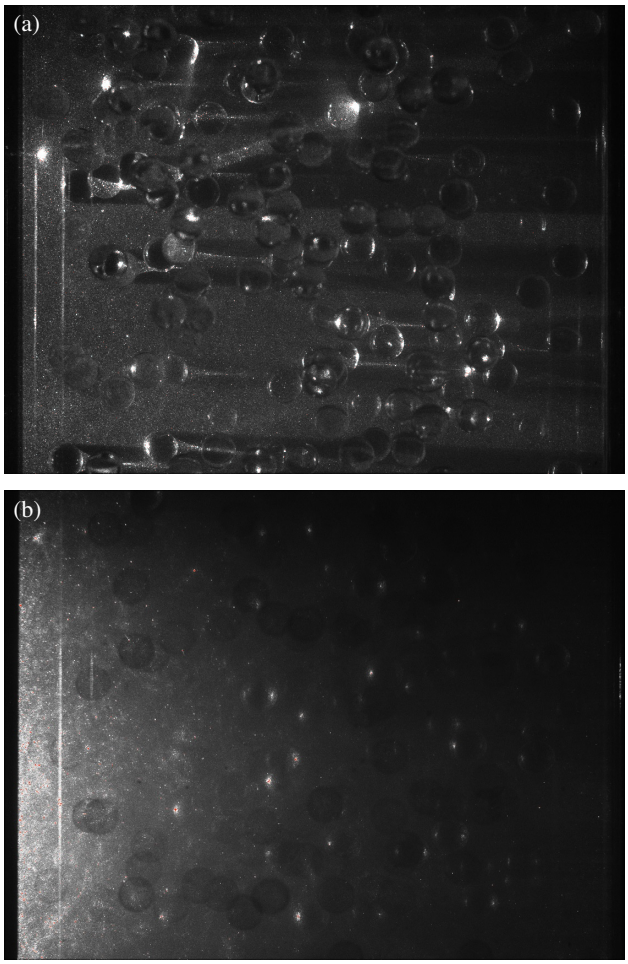

Figure 2: Sample PIV images at 5% v/v bead concentration (a) without refractive-index matching (Glass beads in water) and (b) with refractive-index matching (Borosilicate beads in KSCN).

3. Captured PIV images

Samples of the images obtained in the vertical flow loop with and without refractive-index matching are given in Fig. 2.

Figure 2(a) shows a raw PIV image for the glass-water measurements (no refractive-index matching). It is clear that the slurry beads limit the penetration depth of the laser sheet into the flow by blocking light. In the bead shadows, the seeding particles are not illuminated. There are also several dark regions where no seeding particles are detected. The solid–liquid interfaces generate variation in illumination light intensity due to excessive light flare from the beads, leading to blooming and image saturation denoted by the white regions in the image. The non-uniform distribution of light through phase boundaries due to refraction and reflection is also noticed. The slurry beads create large shadows behind them, which reduce the number of observed seeding particles in those regions. The beads between the laser sheet and the camera also obscure the view. The majority of the image, especially far from the pipe wall, gives no meaningful particle motion information. Finally, a mirror effect at the solid–liquid interface creates ghost particles seemingly inside the solid beads. These issues make it very difficult obtain significant PIV correlation, even with the application of any number of pre-processing filters.

The problems associated with the solid–liquid interface are improved by refractive-index matching. Figure 2(b) represents a typical PIV image obtained using RIM. The image clearly shows a reduction in light flare and light scattering from phase bound-

aries. The RIM technique significantly reduces the shadows cast by the slurry beads. The PIV image has more visible seeding particles, making it possible to measure the velocity of the liquid phase. However, there are still significant challenges to overcome in order to process these PIV images. The edge boundaries between the solid and liquid phase are faint in most of the region but noticeable in some regions of the image. Light is not evenly distributed in the image. The front region where the laser sheet enters the test section has more light. The intensity of light decreases in the radial direction. The background also has nonuniform noise that further creates difficulty in processing such images.

Some of the characteristics of the RIM images described above are universal to these types of measurements, while others are the result of unresolved experimental issues unique to the current dataset. First, the strong decrease in light intensity from the left of the image to the right is due to a pump failure that occurred during testing. Despite affirmations from the manufacturer that the pump would be suitable, we learned that the current combination of bead size, bead rigidity, and corrosive carrier fluid caused the lobe in the pump to deteriorate, causing a black residue to enter the flow and contaminate the fluid. The earlier images look like the one in Fig. 2(b), but the later ones are nearly completely black. We consider the first 1000 images to be reasonable for analysis, while the others are useless. There was also no opportunity to optimize the RIM or imaging systems. After several attempts to resurrect the system, we have determined that a new pump will be required and no further data are available at this time.

Additionally, the bead shadows and remaining bead glare in the image appear to be the result of imperfect RIM. The shadows are the result of the presence of beads just outside of the laser sheet on the camera side and the beads marked by glare are beads just outside of the laser sheet on the opposite side. It is critical that these areas are excluded in the PIV analysis; otherwise the resulting vectors will reflect the bead motion as opposed to the fluid motion. It is hoped that a more careful RIM implementation will reduce these artifacts.

Finally, even without experimental challenges and with perfect RIM, we can expect there to be remaining processing challenges. For example, at every bead location in the image plane, there will be a "black hole" in the image with no seeding particles, and there will be no clearly defined edge, making automated bead detection, tracking, and masking very difficult or impossible. Also, it is likely that at least some artifacts from imperfect RIM will remain and they will have to be identified and treated appropriately. Further thoughts on overcoming these challenges will be given in Sec. 6.

Regardless of the actual effectiveness of RIM for eliminating artifacts, bead detection and masking will still be necessary for PIV in concentrated solid–liquid flows. Since PIV yields evenly spaced vectors on a fixed grid, and masking requires that even a small overlap between a given interrogation window and a masked area make the corresponding vector invalid, a standard PIV implementation would not be effective at isolating the flow around the particle. Furthermore, the fact that the bead moves between the two PIV images would further require that the masked area be bigger, excluding more vectors. For these reasons, we introduce a bead-centric PIV approach that minimizes the excluded image area and obtains resulting PIV vectors on a fixed grid around each bead. This algorithm is described in the next section.

4. Bead-centric PIV processing algorithm

The PIV algorithm used with the current data uses a unique combination of standard techniques to optimize the PIV results available from the challenging RIM-PIV images. The recipe

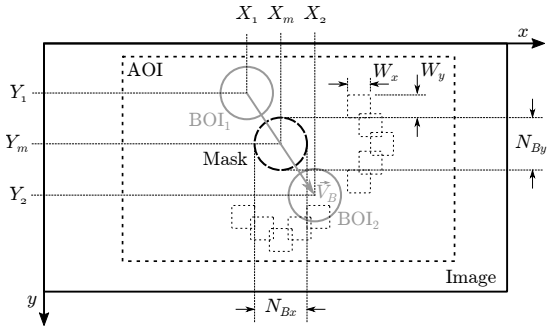

Figure 3: Schematic of BOI image mask, AOI, and some interrogation window locations (small squares)

comprises several steps:

1. Bead registration
2. Interrogation window generation
3. Image pre-processing
4. PIV routine
   - *(i)* Image shifting
   - *(ii)* PIV pass 1
   - *(iii)* Intermediate vector validation
   - *(iv)* Image deformation
   - *(v)* PIV pass 2
5. Vector validation
6. Flow statistics analysis

4.1. Bead registration

Ideally, bead registration would be fully automated. In non-RIM-PIV, it is relatively easy to identify clearly defined bead outlines automatically. However, as RIM effectiveness increases, the outline becomes increasingly faint, and eventually invisible. For the current data set, automated detection was attempted but ineffective. It was determined that a manual detection scheme would be more appropriate. A suggestion to overcome this challenge will be discussed in Sec. 6.

For the registration process only those images for which a clearly defined in-plane Bead of Interest (BOI) with at least some unobstructed surrounding fluid flow that could be identified were used. The aim was to perform PIV on the area immediately surrounding these BOIs; these areas are termed Areas of Interest (AOIs). A graphical user interface for bead registration was developed in MATLAB that allowed BOIs to be precisely located. An AOI was also recorded, which enclosed the BOI and as much of the unobstructed flow field as possible. Any other beads, shadows, glare, or other image artifacts were then selected in both frames as additional beads to be kept for the image masking process in the PIV algorithm. Any other clearly defined in-plane beads were recorded and tagged with a flag denoting that they were in plane. These beads were not used for PIV, but were used for determining the statistics of the solid phase. 250 images were checked for bead registration and 164 (66%) were suitable for the combined bead-tracking/PIV analysis.

4.2. Interrogation window generation

From the point of view of image masking, the appropriate coordinate system for the PIV analysis is a Lagrangian one that follows the BOI. This is because in the BOI's coordinate system, the appropriate image mask does not move, minimizing the number of masked pixels. Figure 3 gives a schematic of the mask coordinates and a sample of some interrogation windows used in the PIV analysis.

The position of the centre of the image mask (X_m, Y_m) in the image coordinates is given by:

$$X_m = \frac{X_1 + X_2}{2}; \quad Y_m = \frac{Y_1 + Y_2}{2}, \tag{1}$$

where (X_1, Y_1) and (X_2, Y_2) are the x- and y-coordinates of the BOI in the first and second image frame, respectively. This is considered to be the bead location at a time midway between the two frames. The diameter of the BOI sets the width and height of the masked area, N_{Bx} and N_{By}, respectively. The width and height of the interrogation window, W_x and W_y, are chosen for each pass before processing as in a typical PIV routine. All of these pixel values must be integers for the PIV correlation to be efficient, so the position values are rounded to the nearest integer, and N_{Bx} and N_{By} are both rounded up to the next integer. A unique and important aspect in this implementation is the selection of interrogation window overlap. In standard PIV, this is normally set *a priori* between 25-75%, but an arbitrary choice here would make it likely that an extra row and column of interrogation windows would overlap the BOI's masked area. The optimal overlaps, l_x and l_y, can be determined by selecting target overlaps, $l_{x,\text{target}}$ and $l_{y,\text{target}}$. Once the target overlaps have been chosen, the number of windows that can fit in the BOI mask can be determined by setting the following conditions: (1) the first window beside the bead mask has no overlap with the mask itself, (2) the first window to have no overlap after passing the BOI mask is as close as possible to the mask edge, (3) an integer number of windows is covered by the BOI mask. According to these conditions, the number of windows that would fit is given by

$$n_{BWx} = \text{nint}\left(\frac{N_{Bx} + 2l_{x,\text{target}}W_x}{W_x\left(1 - l_{x,\text{target}}\right)}\right), \tag{2}$$

$$n_{BWy} = \text{nint}\left(\frac{N_{By} + 2l_{y,\text{target}}W_y}{W_y\left(1 - l_{y,\text{target}}\right)}\right), \tag{3}$$

where nint() is the nearest integer function (rounding). The second term in the numerator comes from the fact that on each side of the BOI, the extent of nearest interrogation window to that edge should extend beyond the bead by the overlap amount so that the edge of the neighbouring interrogation window edge aligns with the edge of the BOI mask. The actual overlap is then given by

$$l_x = 1 - \frac{N_{Bx}}{n_{BWx}W_x}; \quad l_y = 1 - \frac{N_{By}}{n_{BWy}W_y}. \tag{4}$$

The next step is to generate a regular grid of overlapping windows in the AOI using W_x, W_y, l_x, and l_y, which is done for each PIV pass, and the final step is to shift the windows such that the windows that overlap the BOI are centred on the BOI centre. This procedure ensures that the fewest vectors overlap the BOI at all. Any window that overlaps the mask by more than 1% of the total number of pixels in the window is considered invalid. In addition to the BOI mask, the same 1% criterion is applied to any window that overlaps any other masked feature recorded in the bead registration step (*i.e.* other beads or image artifacts). This masking was performed in the BOI's coordinate system for each image frame. Because the window shift in pixels should be an integer for PIV correlation, and it is preferable to keep it the same between each interrogation window, the actual pixel shifts between windows were rounded up to the next pixel. This meant that the actual width or height of the masked area could be up to n_{BWx} and n_{BWy} pixels greater than N_{Bx} and N_{By}, respectively.

4.3. Image pre-processing

To account for nonuniform light intensity in the image, two steps were used. The first step was background subtraction [6], where a background image—obtained by averaging all of the available images—was subtracted from each image. The next step was dynamic histogram stretching [6], applied to 20 × 20 pixel tiles in the image. This step used a contrast-limited adaptive histogram equalization (CLAHE) approach [7]. This was considered to be an effective way to further reduce the contribution of noise from the non-uniform background intensity.

4.4. PIV routine

Though the PIV routine used in this work uses standard processing procedures, the fact that the masks and vector locations changed with each image meant that there was no readily available PIV software with which the processing could be successfully completed. A custom PIV routine was therefore implemented in MATLAB. The code was validated with some test images and compared to two other PIV packages (PIVLab [8] and PIVTEC GmbH's PIVview).

4.4.(i). Image shifting Since the PIV computation is to take place in the BOI's reference frame, it is necessary to first shift each of the image frames to corresponding reference coordinates. This is done symmetrically by shifting each frame by $(X_2 - X_1)/2$ and $(Y_2 - Y_1)/2$ in the appropriate direction. The intermediate images were also stored for later verification.

4.4.(ii). PIV pass 1 The first PIV pass used $W_x = W_y = 64$ px, and l_x and l_y were determined to be 0.69 using Eqn. (4). Any pixels that were in a masked area were also set to zero in each interrogation window. After the calculation was completed, the image frame shift was added back as a pixel shift to the vector values. An FFT-based computation was used. The peak-search routine limited the search to within ± 10 pixels from the expected peak location based on the BOI's velocity.

4.4.(iii). Intermediate vector validation For intermediate outlier detection, a normalized median filter [9] was used, and any vector that deviated by more than five standard deviations from the calculated vectors' mean was also marked as an outlier. Outliers were then replaced by the mean of a 3 × 3 neighbourhood around the vector, excluding any neighbours that were also marked as outliers. Border vectors and those with fewer than three valid neighbours were replaced with the BOI velocity.

4.4.(iv). Image deformation The image deformation was implemented using a symmetric, geometric 2D image deformation calculated as a piece-wise linear transformation field. The field was obtained by defining a set of control point pairs given by $\mathbf{x} - d\mathbf{x}/2$, $\mathbf{y} - d\mathbf{y}/2$ and $\mathbf{x} + d\mathbf{x}/2$, $\mathbf{y}_2 + d\mathbf{y}/2$ where $\mathbf{x}$ and $\mathbf{y}$ are made up of the x- and y-positions of the vectors, respectively, and $d\mathbf{x}$ and $d\mathbf{y}$ are the calculated pixel shifts from the first PIV pass (after vector validation). These intermediate images were also stored.

4.4.(v). PIV pass 2 The second PIV pass used $W_x = W_y = 32$ px, and $l_x = l_y = 0.65$. Again, the same masking and FFT-based computation were used and the local image deformation vector was re-added as a pixel shift to the vector values. The peak-search routine again used a ± 10 pixel limit, this time based on the velocity obtained in the first PIV pass.

4.5. Vector validation

Though not as critical as in the PIV computation steps, it is still important to validate the final vectors before subsequent analysis. Here several criteria were used to identify outliers. Again the normalized median and bulk statistics tests described in Sec. 4.4.(iii) were used, and additionally, any vector for which the peak ratio between the chosen correlation peak and the next peak in the window's interrogation plane was considered an outlier. Outliers that had more than three valid, non-outlier neighbours in their local 3 × 3 neighbourhood were replaced by the local mean of those neighbours. Any outlier that did not satisfy these criteria was tagged as invalid.

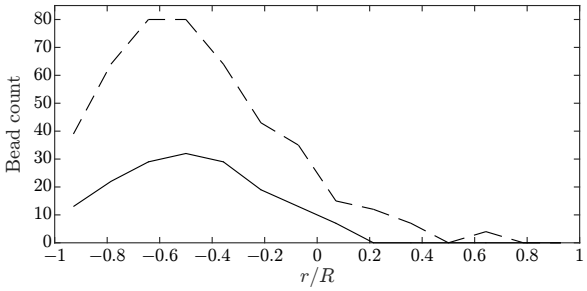

Figure 4: Bead counts for statistical analysis. — BOIs, – – All beads (BOIs + additional beads).

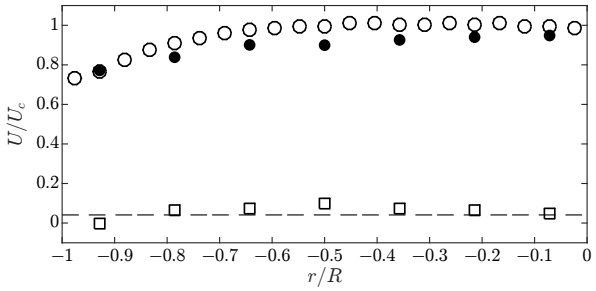

Figure 5: Mean streamwise velocity of each phase. • Solid phase, ○ Liquid phase, □ Slip velocity, – – Terminal settling velocity (calculated).

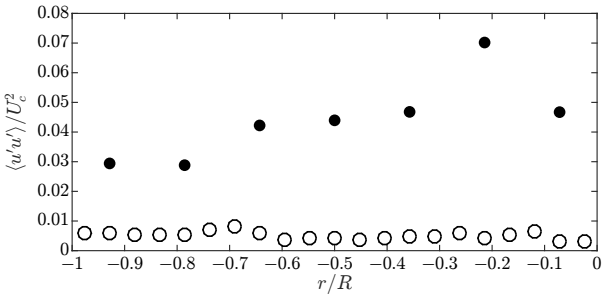

Figure 6: Streamwise fluctuation intensity of each phase. • Solid phase, ○ Liquid phase.

4.6. Data analysis

It should be noted that the BOI selection procedure used in this work introduces a bias to the data that are obtained. Recall that only beads that are clearly identifiable as being in-plane in the images and for which a reasonable amount of fluid flow around the bead was visble could be used as BOIs. This biases the vectors available for the fluid flow analysis toward those that are relatively far from other beads. It also means that the flow snapshots available always coincide with relatively sparse bead distributions in the image. This undoubtedly influences the obtained statistics. Notwithstanding this limitation, we carry on to demonstrate how to obtain the velocity statistics.

To obtain the flow statistics, the pipe was divided into a number of bins in the radial direction: 14 for the solid phase analysis and 42 for the liquid phase. These numbers were chosen so that a reasonable number of BOIs would be available in each bin. The vertical coordinate was ignored. Half of the bins fell between $r/R = -1$ and $r/R = 0$. The histogram in Fig. 4 shows the number of beads used in each bin for the analysis. Very few BOIs were identified for $r/R > 0$ so these results are ignored. The BOI count gives the number of statistically independent snapshots used for the fluid velocity analysis, and the all-bead count gives the number of beads used for the particle velocity analysis.

The procedure for calculating the statistics was straightforward. For each bin, every BOI location that fell in that bin was averaged to determine the average solid phase velocity. The deviations from this average was also recorded to determine the fluctuating statistics. The number of averages used for these statistics is the all-bead line in Fig. 4. Similarly for the liquid phase, for each bin, the vectors associated with valid locations within that bin were summed. Additionally, only those vectors located more than one bead diameter from the edge of the bead were considered valid in this case. This was to isolate the flow of the fluid not in the immediate vicinity of the BOI. Also, to limit the contribution of snapshots that had larger AOIs, a maximum of 25 vectors from each snapshot were used in each bin. These were randomly selected using a random sort routine.

For the fluctuating velocity intensities, the expected velocity for each vector was taken from the mean profile obtained previously. However, instead of using the mean velocity for the entire bin, which would bias the result by allowing variation in the mean profile within the bin to contribute to the fluctuation intensity, an estimate of the local mean velocity at the radial position of each vector was obtained by a linear interpolation of mean profile values from the two nearest bin centres.

For each bin from the solid phase analysis, the average fluid flow field around the beads was obtained by averaging the relative velocity vectors ($\vec{u} - \vec{u}_{\mathrm{BOI}}$) surrounding BOIs that fell in that bin. Only valid vectors were used in the average, which meant that the number of snapshots used for each vector varied from snapshot to snapshot. This number was recorded and any average based on fewer than five valid vectors was excluded.

5. Results and discussion

Figure 5 shows the mean streamwise velocity of each phase in the flow; the radial results are omitted for brevity. The centreline velocity, $U_c = 4.88$ m/s, used for scaling was the average of the fluid vectors used in the bins with centres less than $R/4$ from the centre-line. It is clear that the beads tend to lag the fluid at most locations. This slip velocity is close to the terminal settling velocity for the beads in a quiescent flow, which was 0.041 U_c (determined using a standard drag correlation [10]). Both the slip velocity and the terminal settling velocity are depicted in Fig. 5. Over most of the pipe cross section, the slip velocity is greater than the terminal settling velocity, probably indicating that the effective drag coefficient is reduced by the fluid turbulence. Near the wall, the average bead velocity intersects the average fluid velocity. The trend has been observed previously in more dilute flows [4], and it is likely due to the fact that higher-speed beads moving toward the wall do not have to meet the no-slip condition and can carry their momentum close to the wall.

Figures 6 gives the fluctuation intensities of the streamwise velocities. It appears that the beads have a higher turbulence intensity than the fluid and that the turbulence intensity distribution is relatively constant throughout the pipe radius. However, due to the small number of averages available, and the abovementioned issue of biasing introduced by manual BOI selection, drawing further conclusions from these results or comparing them directly to single-phase results does not seem warranted.

Finally, of particular interest is Fig. 7, which shows the average flow field around the BOIs for each bin. Again, the vectors are relative to the BOI velocity. For the most part, we can see that the average flow around the bead is upward, reflecting the positive slip velocity observed at most locations in Fig. 5. Also, in the first two bins, we see a greater velocity for positive x_{Rel}/R_B (the x-position relative to the BOI divided by the bead radius), which illustrates the expected mechanism of near-wall lift, and there is a significant variation in wake shape at the various bin locations.

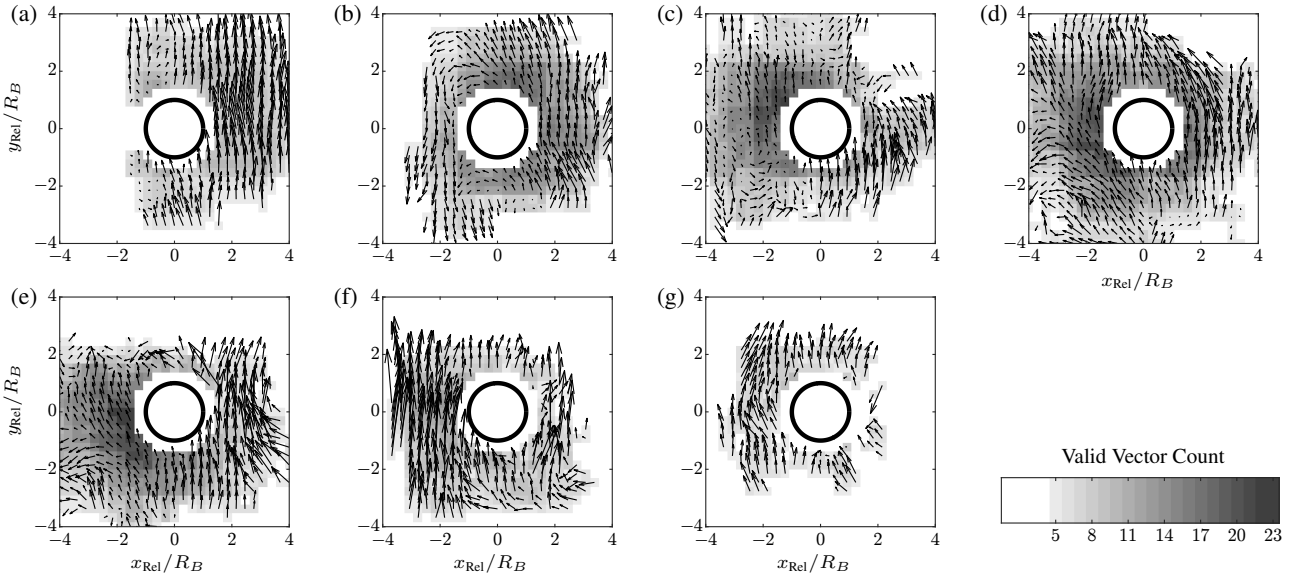

Figure 7: Mean flow field around BOIs for bin (a) $-1 \leq r/R < -0.86$, (b) $-0.86 \leq r/R < -0.71$, (c) $-0.71 \leq r/R < -0.57$, (d) $-0.57 \leq r/R < -0.43$, (e) $-0.43 \leq r/R < -0.29$, (f) $-0.29 \leq r/R < -0.14$, and (g) $-0.14 \leq r/R < 0$. The background shading gives the valid vector count used in each average vector.

6. Conclusion

This paper has introduced a procedure for bead-centric PIV of refractive-index-matched high-concentration solid–liquid flows. Though a pump failure meant that only one test condition with a relatively small number of images was available, this paper shows both steps that are necessary to obtain PIV vectors from RIM images in concentrated solid–liquid flows as well as preliminary results of the mean and fluctuating velocity statistics. The mean flow results show that the solid beads lag the fluid flow in the central pipe region by an amount close to the terminal settling velocity of the beads. The bead velocity matches and even exceed the liquid velocity close to the wall. The mean flow around the beads in a Lagrangian reference frame at various radial locations has also been obtained for the first time, demonstrating qualitatively the mechanism of near-wall lift near the wall and showing the bead wakes. Because of the low statistical power of the averages due to the small number of available images, further quantitative analysis and comparison have not been performed.

The next step will be to automate the bead registration process and use the technique on a much larger number of images. Automating this process is made difficult by the fact that the bead edges are very faint in the images, which is a logical result of refractive-index matching. To overcome this, we recommend altering a certain portion of the beads such that they have the same dynamic properties but are optically distinguishable from the flow. Options include the use of an opaque or fluorescent coating or the use of beads with a different refractive index. Examples of such techniques are available in the literature [11].

These results show the promise of the bead-centric PIV procedure introduced here. It is hoped that with a minor improvements and careful application of the technique, a clear investigation of the statistics of high-concentration solid–liquid flows will be possible.

References

[1] Gore, R. A. and Crowe, C. T., Effect of particle size on modulating turbulent intensity, *International Journal of Multiphase Flow*, pp. 279–285, 1989.

[2] Tanaka, T. and Eaton, J. K., Classification of turbulence modification by dispersed spheres using a novel dimensionless number, *Physical Review Letters*, p. 114502, 2008.

[3] Balachandar, S. and Eaton, J. K., Turbulent dispersed multiphase flow, *Annual Review of Fluid Mechanics*, pp. 111–133, 2010.

[4] Shokri, R., Ghaemi, S., Nobes, D. S., and Sanders, R. S., Investigation of particle-fluid interaction at high reynolds-number using PIV/PTV techniques, *Proceedings of the International Symposium on Turbulence and Shear Flow Phenomena (TSFP-9)*, Melbourne, Australia, 2015.

[5] Agrawal, Y. K., Shokri, R., Sanders, R. S., and Nobes, D. S., Turbulence statistics in solid-liquid flow using a refractive index matching and particle image velocimetry technique, *Proceedings of the 10th Pacific Symposium on Flow Visualization and Image Processing*, Naples, Italy, 2015.

[6] Raffel, M., Willert, C. E., Wereley, S., and Kompenhans, J., *Particle Image Velocimetry: A Practical Guide*, 2 ed., Springer, Berlin, 2007.

[7] Shavit, U., Lowe, R. J., and Steinbuck, J. V., Intensity capping: a simple method to improve cross-correlation PIV results, *Experiments in Fluids*, pp. 225–240, 2006.

[8] Thielicke, W. and Stamhuis, E., PIVlab – Towards user-friendly, affordable and accurate digital particle image velocimetry in MATLAB, *Journal of Open Research Software*, 2, 2014.

[9] Westerweel, J. and Scarano, F., Universal outlier detection for PIV data, *Experiments in Fluids*, pp. 1096–1100, 2005.

[10] Clift, R., Grace, J. R., and Weber, M. E., *Bubbles, drops, and particles*, Academic Press, New York, 1978.

[11] Cui, M. M. and Adrian, R. J., Refractive index matching and marking methods for highly concentrated solid–liquid flows, *Experiments in Fluids*, pp. 261–264, 1997.